Microscopic origins of hydrodynamic transport in the type-II Weyl semimetal WP_2

Jennifer Coulter,[1,*] Ravishankar Sundararaman,[2] and Prineha Narang[1,†]
[1]*John A. Paulson School of Engineering and Applied Sciences, Harvard University, Cambridge, Massachusetts 02138, USA*
[2]*Department of Materials Science and Engineering, Rensselaer Polytechnic Institute, Troy, New York 12180, USA*

(Received 4 June 2018; revised manuscript received 31 July 2018; published 19 September 2018)

A microscopic understanding of hydrodynamic transport in Dirac and Weyl semimetals has remained elusive in theoretical descriptions and experimental measurements. We investigate the structure and microscopic properties of transport in WP_2, a type-II Weyl semimetal exhibiting hydrodynamic transport. Here, we characterize the nature of the microscopic properties of WP_2 as a function of temperature through *ab initio* calculations of the relevant scattering processes, including electron-phonon and electron-electron lifetimes, and provide equivalent calculations for copper as a point of reference. Additionally, we present an approach to calculate phonon drag, a mechanism invoked in recent experiments, through predictions of a phonon-mediated electron-electron lifetime. We show that the resistivity is very well described by the electron-phonon interaction alone, indicating WP_2 exhibits conventional metallic electrical behavior in which strong electron-electron correlations do not play a significant role. After establishing the zone-averaged behavior of the calculated lifetimes, we further investigate specific features of the spatial distribution of the electron-phonon lifetime across the Fermi surfaces of WP_2 to study possible scattering channels involved in hydrodynamic transport and quantify the degree of lifetime anisotropy in electron and hole pockets. This description of microscopic dynamics in WP_2 prompts additional investigation of specific scattering channels and indicates the importance of phonon interactions in understanding connections between transport in hydrodynamic materials and strongly correlated systems including unconventional metals.

DOI: 10.1103/PhysRevB.98.115130

I. HYDRODYNAMIC TRANSPORT

In conventional materials under the influence of an applied field, electronic transport can be generally understood in terms of Ohmic physics. However, in graphene at charge neutrality, and more recently, a number of semimetallic compounds, electrons in a sample can behave as a viscous fluid described not by Ohmic physics, but through the formalism of hydrodynamics. In this regime, electrons move through a two-dimensional (2D) plane of a sample in a fashion loosely analogous to water flowing through a pipe.

In the language of microscopic interparticle scattering, the appearance of a hydrodynamic regime implies momentum-conserving (MC) processes such as electron-electron and some electron-phonon processes occurs far more often than momentum-relaxing (MR) processes including defect, boundary, and Umklapp scattering, resulting in a separation of MC and MR time scales. Since MR scattering occurs very slowly relative to MC scattering, momentum is considered to be "quasiconserved," and the relevant conservation equations of hydrodynamics can be used to describe transport.

Such hydrodynamic effects have been studied extensively in graphene [1–6]. However, recent experimental studies have revealed similar signatures in layered metal $PdCoO_2$ [7], and Dirac semimetal $PtSn_4$ [8], and type-II Weyl semimetal tungsten phosphide (WP_2). In these newly identified materials, a number of theoretical questions remain in regard to the microscopic interactions that drive a transition to the hydrodynamic regime. Ongoing discussion centers around similarities in the crystal structure and Fermi surfaces of WP_2, $PdCoO_2$, and $PtSn_4$ [7–9], the impact of phonon drag and other thermoelectric effects, related deviations from the Wiedemann-Franz law [10], and the significance of electron-phonon interactions including the potential importance of small-angle scattering to the onset of hydrodynamic flow [8].

To address these questions, we present a direct evaluation of the microscopic scattering rates in WP_2 using *ab initio* calculations of the electron and phonon states to study electron-phonon coupling in the material. We evaluate relevant scattering rates, such as those for electron-electron and electron-phonon processes, in addition to the momentum relaxing scattering rates measured in experiment. From these calculations, we present a microscopic perspective of scattering in WP_2.

II. COMPUTATIONAL METHODS

WP_2 forms a bulk orthorhombic ($Cmc2_1$) structure and manifests four pairs of type-II Weyl points in the $k_z = 0$ plane [11,12]. In experimental transport measurements, WP_2 is considered quasi-2D as a result of strong magnetotransport anisotropy which favors flow in the a-c crystal plane, similar to anisotropy observed in $PdCoO_2$ and $PtSn_4$ [9].

Figure 1 shows the crystal structure, the calculated electron and phonon band structures, and indicates the location of Weyl points in the Brillouin zone. In our calculations, we

*jcoulter@g.harvard.edu
†prineha@seas.harvard.edu

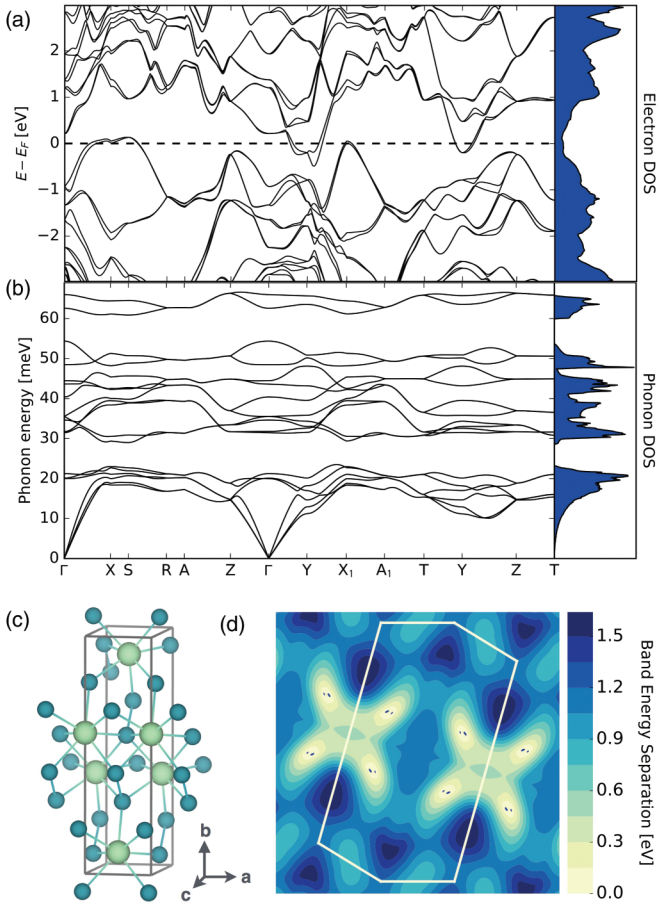

FIG. 1. Electronic structure and phonon dispersion of WP_2. (a) Electronic band structure and (b) phonon dispersion, with corresponding densities of states, for the orthorhombic WP_2 structure shown in (c) calculated using fully relativistic *ab initio* calculations (including self-consistent spin-orbit coupling). (d) Four pairs of Weyl points emerge from electronic structure predictions. Here, the contour levels indicate the energy separation of the two crossing bands, with areas of separation less than 0.02 eV in dark blue to identify the Weyl points.

locate a pair of Weyl points at $[k_x, k_y] = [-0.282, 0.302]$ and $[-0.238, 0.283](1/\text{Å})$ at energies of -0.504 and -0.301 eV, respectively, showing our electronic structure agrees with experimental reports [11,12] with all eight Weyl points visible in the contour map of Fig. 1(d).

From these electron and phonon states, we calculate electron-phonon and electron-electron scattering rates ($2\hbar\times$ corresponding imaginary part of self-energy) using Fermi's golden rule and the random-phase approximation, respectively, following our previously established methodology [13–17]. We calculate net transport coefficients including resistivity and mobility based on the linearized Boltzmann equation with an all-bands relaxation-time approximation [15].

Additionally, we evaluate a lifetime associated with phonon drag, a mechanism discussed as an additional source of MC scattering which is considered beneficial to the onset of hydrodynamic transport. We estimate a phonon drag contribution using the rate of electron-electron scattering mediated by a virtual phonon, rather than the conventional Coulomb-mediated scattering. Within the random-phase approximation, we find

$$\left(\tau_{\text{ee}}^{\text{ph}}\right)^{-1} = \frac{\pi\beta\hbar^2}{2g(\varepsilon_F)}\sum_{\alpha}\int\frac{\Omega \mathrm{d}\vec{q}}{(2\pi)^3}G_{\vec{q}\alpha}^2 \times\int_{-\infty}^{\infty}\frac{\omega^2 \mathrm{d}\omega}{|\bar{\omega}_{\vec{q}\alpha}-\omega|^2\sinh^2\frac{\beta\hbar\omega}{2}}, \tag{1}$$

where $\bar{\omega}_{\vec{q}\alpha} = \omega_{\vec{q}\alpha}(1 + i\pi G_{\vec{q}\alpha})$ are complex phonon frequencies including the linewidth due to phonon-electron scattering, $\beta = (k_B T)^{-1}$, and $g(\varepsilon_F)$ is the density of states at the Fermi level. Above,

$$G_{\vec{q}\alpha} \equiv \sum_{ab}\int\frac{\Omega \mathrm{d}\vec{k}}{(2\pi)^3}\left|g_{\vec{k}a,(\vec{k}+\vec{q})b}^{\vec{q}\alpha}\right|^2\delta(\varepsilon_{\vec{k}a}-\varepsilon_F)\delta(\varepsilon_{(\vec{k}+\vec{q})b}-\varepsilon_F), \tag{2}$$

is the weight of each phonon mode in the Eliashberg spectral function, calculated from first-principles electron energies $\varepsilon_{\vec{k}a}$ and electron-phonon matrix elements $g_{\vec{k}a,\vec{k}'b}^{\vec{q}\alpha}$ (see appendix for further details).

All quantities are derived from relativistic *ab initio* calculations with self-consistent spin-orbit coupling and implicitly treat processes such as Umklapp scattering [15].

III. SCATTERING RATES AND TRANSPORT PROPERTIES FROM FIRST PRINCIPLES

Hydrodynamic transport requires MC scattering rates to dominate over MR scattering rates (i.e., correspondingly $\tau^{\text{MC}} \ll \tau^{\text{MR}}$), conventionally ascribed to electron-electron (ee) and electron-phonon (e-ph) scattering, respectively. From our calculations, we can directly evaluate the contributions of various microscopic mechanisms to MC and MR scattering, as shown in Fig. 2(a).

The calculated electron-phonon MR scattering time $\tau_{\text{e-ph}}^{\text{MR}}$ is in excellent agreement with experimental data [9], implying that our computational methods correctly capture the physics of this material. Some separation from experiment occurs at 2 K, where it is likely that small effects from defects or sample boundaries, which are not present in an idealized electronic structure calculation, could contribute to MR scattering and cause discrepancy between prediction and experiment. However, there is experimental evidence of both Wiedemann-Franz deviation [18] and possible hydrodynamic behavior at 10 K [9], where our theory and experiment match well. This indicates that our methods remain predictive throughout the regime of interest.

While we find this strong agreement with experiment, we also determine that contrary to current understanding of hydrodynamic transport in graphene, the predicted Coulomb mediated electron-electron scattering time is much longer than other processes over most of the temperature range, indicating that it cannot be the mechanism of MC scattering responsible for hydrodynamic behavior in WP_2.

We instead predict that phonons dominate the momentum-conserving scattering processes. At temperatures below 100 K, overall electron-phonon scattering (with time $\tau_{\text{e-ph}}$) is much faster than its momentum-relaxing component (with

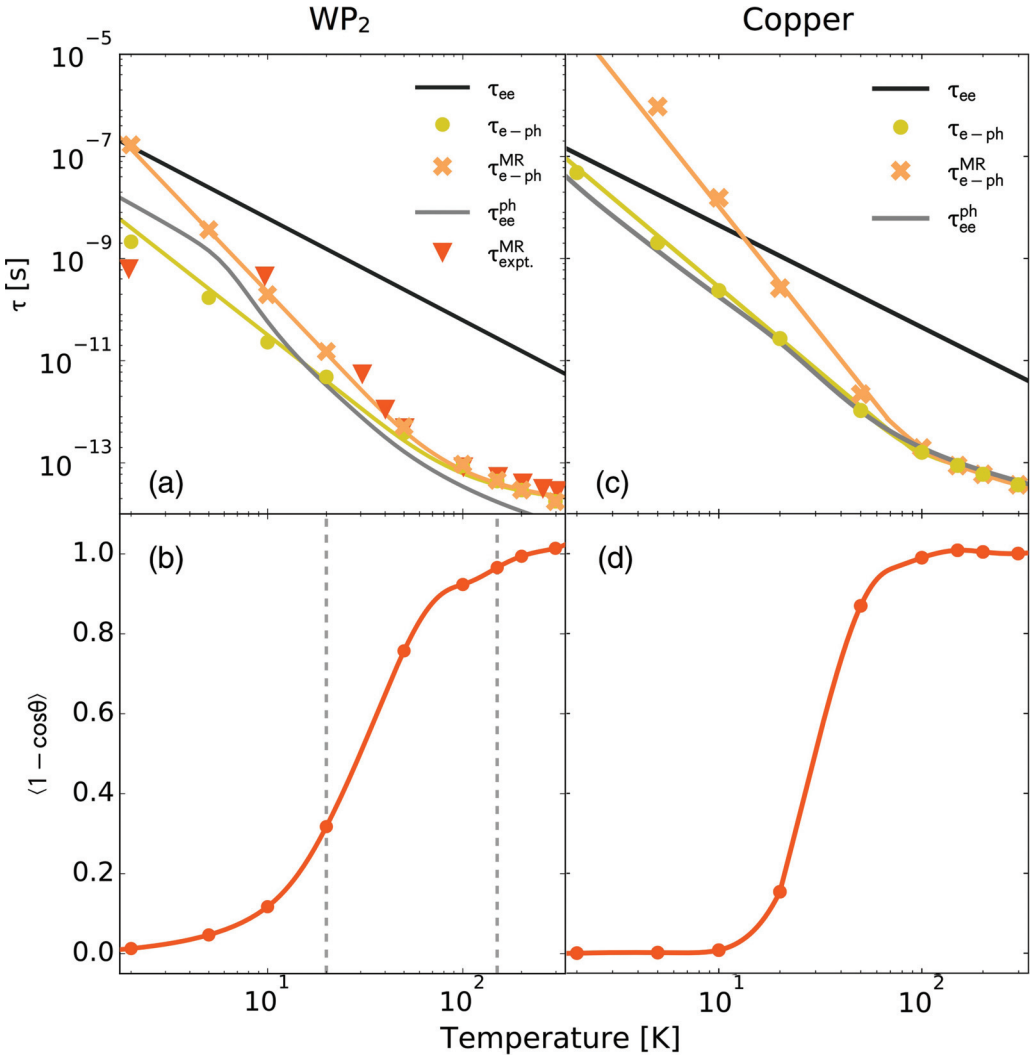

FIG. 2. Predicted temperature dependent lifetimes to distinguish the momentum-relaxing and momentum conserving processes. (a) Calculations for WP_2 reveal that the momentum-relaxing electron-phonon (e-ph) scattering time $\tau^{MR}_{e\text{-}ph}$, is in agreement with experiment τ^{MR}_{expt} [9], and is longer than the total e-ph scattering time $\tau_{e\text{-}ph}$. The Coulomb-mediated electron-electron (ee) scattering time τ_{ee} is much longer than the phonon-mediated ee scattering time τ^{ph}_{ee}. Phonons determine both the MC and MR processes in WP_2, in contrast to previous hydrodynamic materials like graphene, where the electron-electron interaction is considered as the dominant source of MC scattering. (b) Probability of momentum relaxation by e-ph scattering $\langle 1 - \cos\theta \rangle$ drops off with decreasing temperatures (small-angle scattering increases). Dashed lines denote where experiment [9] reports onset of a "hybrid" ballistic/hydrodynamic regime at 150 K and "pure" hydrodynamics at 20 K. (c) and (d) The same calculations for copper to highlight the faster e-ph rates in WP_2 and also the behavioral difference in τ^{ph}_{ee}.

time $\tau^{MR}_{e\text{-}ph}$). This is because low energy acoustic phonons that dominate scattering at lower temperatures predominantly change the electron momenta by small angles, as shown by the average value of $\langle 1 - \cos\theta \rangle$ dramatically reducing in magnitude with decreasing temperature in Fig. 2(b). Within a Debye model for the scattering time, $\tau_{e\text{-}ph} \propto T^{-4}$ and $\tau^{MR}_{e\text{-}ph} \propto T^{-5}$ for $T \ll T_D$, the Debye temperature, while both are $\propto T^{-1}$ for $T \gg T_D$. Figure 2(a) also shows the excellent Debye model fits to the *ab initio* predictions for $\tau_{e\text{-}ph}$ and $\tau^{MR}_{e\text{-}ph}$, confirming the acoustic phonon energy explanation for small-angle scattering.

To understand WP_2 in comparison to traditional metals, we present an identical set of calculations for copper in Fig. 2. We can see the lifetimes for WP_2 and copper follow similar trends, as both exhibit the expected temperature dependence for electron-phonon lifetimes in metals. We note that the total e-ph and MR e-ph lifetimes in WP_2 are several orders of magnitude smaller than in copper, indicating that the electron-phonon coupling in WP_2 is somewhat stronger than in copper.

Additionally, we find that phonon-mediated electron-electron scattering times, representative of a MC phonon drag scattering rate, also dominate conventional Coulomb-mediated electron-electron scattering. We observe a potentially interesting feature of the phonon drag lifetime. As temperature decreases, the phonon drag scattering rate slows near ∼10 K in Fig 2(a). In Fig. 2(c), we can see that this behavior does not appear in copper.

We also evaluate the conductivity tensor from first principles, shown in Fig. 3, where we present the calculated resistivity overlaid with the corresponding experimental data,

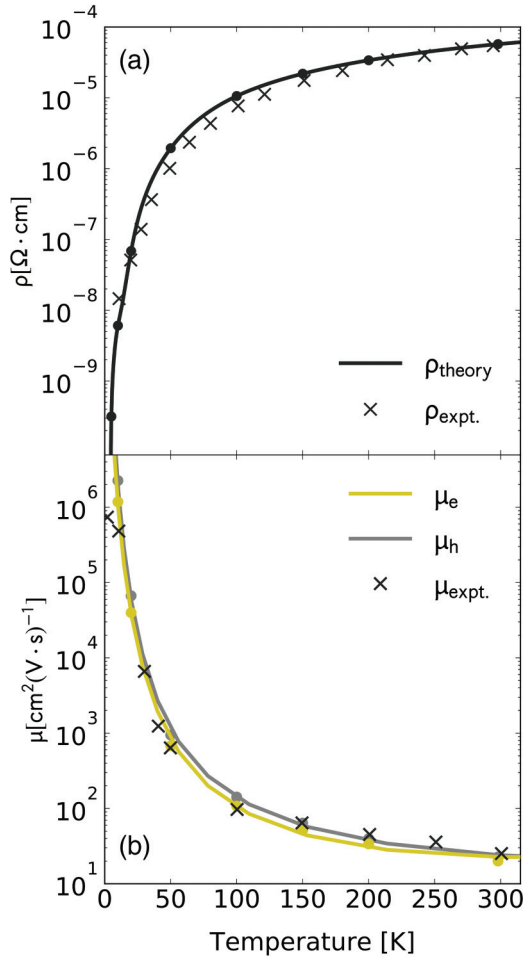

FIG. 3. Transport from first-principles. *Ab initio* calculation of the conductivity tensor from a linearized Boltzmann equation with a full-band relaxation-time approximation predicts (a) resistivity and (b) mobilities, in excellent agreement with experiment [9,19]. This agreement establishes the reliability of first-principles predictions of lifetimes in this material and strongly indicates that electron-electron scattering is not a dominant contributor to electrical conductivity in WP_2.

with mobility from Ref. [9] and resistivity from [19]. For both of these calculated transport properties, we find that our calculations are in excellent agreement with experimental reports presented as a function of temperature, indicating that our methods appropriately describe the microscopic properties of this material. Again, this strongly suggests that Coulomb mediated electron-electron interactions do not dominate the transport in WP_2, as in systems where electron-electron scattering is very strong, the electrical conductivity would not be reproducible from e-ph interactions alone.

IV. FEATURES OF THE ELECTRON-PHONON LIFETIME RESOLVED FERMI SURFACE

To study the distribution of lifetimes across the Brillouin zone with the aim of better understanding the importance of specific scattering mechanisms in WP_2, we project the calculated electron-phonon lifetime values across the Fermi surface.

The basic form of these surfaces is consistent with the "bowtie" electron and quasi-2D "tube" hole pockets observed via ARPES [12,20]. As shown in Fig. 4(a), there are two bands associated with each of the hole and electron pockets as a result of the strong spin-orbit coupling in WP_2.

At low temperatures, the hole pockets, which determine the magnetotransport anisotropy for WP_2, feature particularly high lifetime $\tau_{e\text{-}ph}$ regions, as shown in Fig. 4(d).

High lifetimes over most of the Fermi surface at low temperatures is typical for conventional metals (see appendix for comparison to copper). However, the appearance of such long-lived states, to the extreme that at 2 K the longest and shortest lived states are separated by 6 orders of magnitude, is noteworthy.

In addition to the observation of these particularly long-lived states on the hole pockets, we also include a series of distributions of $\tau_{e\text{-}ph}$ over the hole and electron pockets in Fig. 4(b), as well as the ratio of the maximum and minimum lifetime values on the hole and electron pockets to quantify how the distribution of lifetimes changes with temperature in Fig. 4(c). We find that between 20 and 50 K the overall shape of the distributions changes, and these long-lived states appear in the tail of the distributions of the hole pockets in Fig. 4(c). It is worth noting that the change in the distribution of lifetimes corresponds to the temperature range in which the electron-phonon scattering angle in Fig. 2(b) shifts to nearly all small-angle scattering.

These results, along with recent discussion suggesting Wiedemann-Franz departure in WP_2 could stem from abundant small-angle scattering [18], warrant a deeper investigation of specific scattering mechanisms in WP_2 and similar materials. In addition, while we find WP_2 to be a well-behaved Fermi liquid, the unusual distribution of lifetimes across the Brillouin zone is reminiscent of theoretical work on Wiedemann-Franz violation and scattering of long-lived "cold" states in non-Fermi liquid systems [10], and indicates that future investigation should further probe the nature of available scattering states in hydrodynamic materials.

V. CONCLUSIONS

These predictions present a microscopic perspective of the role of scattering in a system exhibiting hydrodynamic transport. The study of electron-phonon coupling and related scattering rates in WP_2 shows that phonon-related processes, rather than purely electron-electron processes, play a critical role in the emergence of hydrodynamic behavior. Agreement of our theoretical predictions with experimental measurements of resistivity indicate that the electrical properties of WP_2 are indeed dominated by electron-phonon processes, and suggest that strong electronic correlations are not present in this material.

In addition to the zone-averaged lifetimes presented in comparison to experiment, calculated Fermi surface projected lifetimes show a distinct departure from behavior in traditional metals such as copper, making further investigation of scattering effects near E_F imperative. The prediction of unusually long-lived states and severely anisotropic electron-phonon lifetimes at low temperatures is particularly interesting in the context of current understanding of Wiedemann-Franz

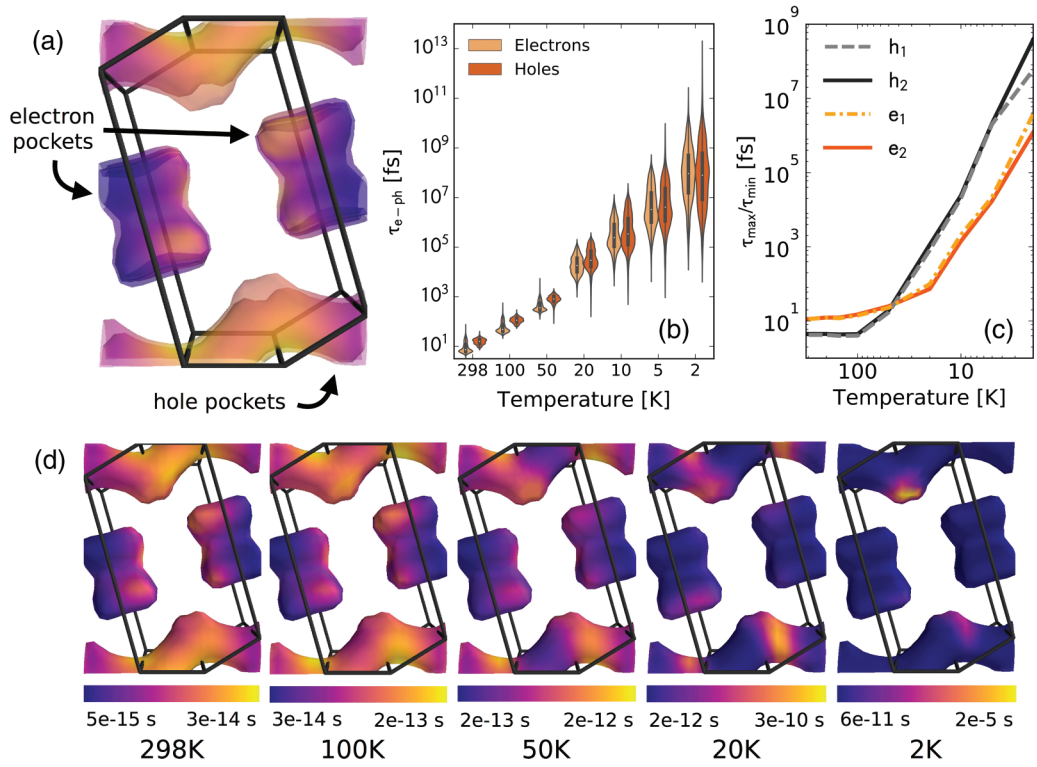

FIG. 4. Anisotropic electron-phonon lifetime across the Fermi surface. The degree of anisotropy, and especially the difference between bowtie-shaped electron pockets and tube-shaped hole pockets strongly increases with decreasing temperature, as shown here. In (a) we show that there are two bands which appear one inside the other as a result of spin-orbit coupling. In (b), we show the distribution of the electron-phonon lifetimes for the bands associated with the hole and electron pockets at each calculated temperature. The overall shape of the distribution changes between 20 and 50 K, and below 20 K, the maximum values of the hole pocket lifetime distributions continue to increase, representing the emergence of high lifetime regions. (c) Shows the ratio of the maximum and minimum values of $\tau_{e\text{-}ph}$ on the hole and electron pocket bands to further highlight the large variation of predicted lifetimes as well as the distinct difference in range between the hole and electron pockets. Importantly, we see a change between the calculated points at 20 and 50 K, identifying the Fermi-surface linked features of hydrodynamic transport, which is reported to fully onset at 20 K. In (d) we visualize the appearance of the high lifetime regions across the Fermi surface with decreasing temperature.

violation in WP_2, and may present an avenue to connect hydrodynamic materials and strongly correlated systems. Understanding the full implications of this effect could strengthen the growing link between hydrodynamic materials and transport behavior in unconventional metals.

Further, from our calculations of a scattering rate representing phonon drag, a normal, intravalley electron-electron scattering rate involving primarily small wave-vector phonons, and the apparent slowing of this rate around 15 K, we also propose that competition for small wave-vector phonons could emerge in this material at low temperatures. This, in conjunction with our observation of very long-lived states at E_F, may imply a mechanism such as phonon bottleneck, in which electrons lack available small wave-vector phonons to relax fully, resulting in slowed electronic relaxation and impaired heat dissipation, could play a role in this system. This result motivates deeper consideration of the semimetallic band structure and Fermi surface character of the recently investigated hydrodynamic compounds.

This work also serves as a foundation for further study of scattering rates in hydrodynamic materials. Predictions of phonon lifetimes, thermal conductivity, and the contributions of the electronic and lattice components of thermal properties of WP_2 could be used to understand the breakdown of the Wiedemann-Franz law through joint calculations of thermal and electrical properties. Going forward, we hope the present methods could be extended to a fully first-principles framework for the identification of new hydrodynamic materials.

ACKNOWLEDGMENTS

This research used resources of the National Energy Research Scientific Computing Center, a DOE Office of Science User Facility supported by the Office of Science of the U.S. Department of Energy under Contract No. DE-AC02-05CH11231, as well as resources at the Research Computing Group at Harvard University. J.C. recognizes the support of the DOE Computational Science Graduate Fellowship (CSGF). R.S. acknowledges start-up funding from the Department of Materials Science and Engineering at Rensselaer Polytechnic Institute. P.N. acknowledges start-up funding from the Harvard John A. Paulson School of Engineering and Applied Sciences. The authors thank Amir Yacoby, George Varnavides, and Chris Ciccarino for helpful discussions. J.C. and P.N. acknowledge support from

the STC Center for Integrated Quantum Materials NSF Grant No. DMR-1231319.

APPENDIX

1. Lifetime Evaluation

We use first-principles density-functional theory calculations of electrons, phonons, and their coupling matrix elements in the open-source JDFTX software [13]. To accurately and self-consistently capture the strong spin-orbit effects present in WP_2, our calculations employ fully relativistic ultrasoft pseudopotentials [21,22] for the PBEsol exchange-correlation functional [23]. We obtain well-converged results for a $6 \times 6 \times 4$ k-point mesh, a plane-wave energy cutoff of 25 E_h (Hartrees), Fermi-Dirac smearing with 0.01 E_h width, and a $3 \times 3 \times 2$ phonon supercell.

From these electron and phonon states, using a basis of maximally localized Wannier functions that covers electronic bands up to $\sim$10 eV above the Fermi level, we interpolate all *ab initio* energies and matrix elements to substantially finer electron and phonon wave-vector meshes ($\sim 10^4$–$\sim 10^6$ wave vectors from high to low temperature) for the subsequent perturbation theory results discussed below.

a. Electron-phonon lifetime

From these initial DFT calculations, we then calculate an *ab initio* temperature-dependent electron-phonon lifetime using Fermi's golden rule [15]:

$$(\tau_{\text{e-ph}})^{-1}_{\mathbf{k}n} = \frac{2\pi}{\hbar}\int_{\text{BZ}} \frac{\Omega d\mathbf{k}'}{(2\pi)^3} \sum_{n'\alpha\pm} \delta(E_{\mathbf{k}'n'} - E_{\mathbf{k}n} \mp \hbar\omega_{\mathbf{k}'-\mathbf{k},\alpha}) \times \left(n_{\mathbf{k}'-\mathbf{k},\alpha} + \frac{1}{2} \mp \left(\frac{1}{2} - f_{\mathbf{k}'n'}\right)\right) \left|g^{\mathbf{k}'-\mathbf{k},\alpha}_{\mathbf{k}'n',\mathbf{k}n}\right|^2 \quad \text{(A1)}$$

where g is the electron-phonon transition matrix element, $\vec{k}$ represents a wave vector in the Brillouin zone, n represents an electronic band index, and α a phonon polarization index. We then report the Fermi-surface averaged $\tau_{\text{e-ph}}$, weighted by the square of the velocity since that determines contribution to electron transport, given by

$$\tau_{\text{e-ph}} = \frac{\int_{\text{BZ}} \frac{d\mathbf{k}}{(2\pi)^3} \sum_n \frac{\partial f_{\mathbf{k}n}}{\partial \varepsilon_{\mathbf{k}n}} |v_{\mathbf{k}n}|^2 (\tau_{\text{e-ph}})_{\mathbf{k}n}}{\int_{\text{BZ}} \frac{d\mathbf{k}}{(2\pi)^3} \sum_n \frac{\partial f_{\mathbf{k}n}}{\partial \varepsilon_{\mathbf{k}n}} |v_{\mathbf{k}n}|^2}. \quad \text{(A2)}$$

b. Momentum-relaxing electron-phonon lifetime

The momentum-relaxing scattering time is also calculated using Fermi's golden rule, similarly to the electron-phonon lifetime but additionally accounting for the relative change in momentum based on the scattering angle between final and initial states [15],

$$\left(\tau^{\text{MR}}_{\text{e-ph}}\right)^{-1}_{\mathbf{k}n} = \frac{2\pi}{\hbar}\int_{\text{BZ}} \frac{\Omega d\mathbf{k}'}{(2\pi)^3} \sum_{n'\alpha\pm} \delta(E_{k'n'} - E_{\mathbf{k}n} \mp \hbar\omega_{\mathbf{k}'-\mathbf{k},\alpha}) \times \left(n_{\mathbf{k}'-\mathbf{k},\alpha} + \frac{1}{2} \mp \left(\frac{1}{2} - f_{\mathbf{k}'n'}\right)\right) \left|g^{\mathbf{k}'-\mathbf{k},\alpha}_{\mathbf{k}'n'}\right|^2 \times \left(1 - \frac{v_{\mathbf{k}n} \cdot v_{\mathbf{k}'n'}}{|v_{\mathbf{k}n}||v_{\mathbf{k}'n'}|}\right). \quad \text{(A3)}$$

As before, we then report the Fermi-surface averaged $\tau^{\text{MR}}_{\text{e-ph}}$ weighted by the square of the velocity, given by

$$\tau^{\text{MR}}_{\text{e-ph}} = \frac{\int_{\text{BZ}} \frac{d\mathbf{k}}{(2\pi)^3} \sum_n \frac{\partial f_{\mathbf{k}n}}{\partial \varepsilon_{\mathbf{k}n}} |v_{\mathbf{k}n}|^2 \left(\tau^{\text{MR}}_{\text{e-ph}}\right)_{\mathbf{k}n}}{\int_{\text{BZ}} \frac{d\mathbf{k}}{(2\pi)^3} \sum_n \frac{\partial f_{\mathbf{k}n}}{\partial \varepsilon_{\mathbf{k}n}} |v_{\mathbf{k}n}|^2}. \quad \text{(A4)}$$

c. Electron-electron lifetime

We calculate the electron-electron lifetime from the imaginary part of the electron self-energy within the random phase approximation (RPA) as

$$\left(\tau^{ee}_{\mathbf{k}n}\right)^{-1} = \frac{2\pi}{\hbar}\int_{\text{BZ}} \frac{d\mathbf{k}'}{(2\pi)^3} \sum_{n'} \sum_{GG'} \tilde{\rho}_{\mathbf{k}'n',\mathbf{k}n}(G) \tilde{\rho}^*_{\mathbf{k}'n',\mathbf{k}n}(G') \times \frac{1}{\pi} \text{Im}\left[\frac{4\pi e^2}{|\mathbf{k}' - \mathbf{k} + G|^2} \varepsilon^{-1}_{GG'}(\mathbf{k}' - \mathbf{k}, \varepsilon_{\mathbf{k}n} - \varepsilon_{\mathbf{k}'n'})\right], \quad \text{(A5)}$$

where $\tilde{\rho}_{\mathbf{k}'n',\mathbf{k}n}$ are the density matrices expressed in the plane-wave basis and $\varepsilon_{GG'}(\mathbf{k}' - \mathbf{k}, \varepsilon_{\mathbf{k}n} - \varepsilon_{\mathbf{k}'n'})$ is the RPA dielectric function. See Ref. [15] for further details.

To determine the temperature dependence of τ_{ee}, we need to rely on an analytical correction to the above-calculated values due to the difficulty in directly calculating τ_{ee} on a fine-enough mesh to get sufficient states within $k_B T$ of the Fermi surface at room temperature. Because the density of states for WP_2 does not vanish at ε_F, conventional Fermi-liquid theory relations should apply near ε_F. In Fermi-liquid theory, the electron-electron scattering rate grows quadratically away from the Fermi energy and with temperature, proportional to

$$\tau^{-1}_{ee}(\varepsilon, T_e) \approx \frac{D_e}{\hbar}[(\varepsilon - \varepsilon_F)^2 + (\pi k_B T_e)^2]. \quad \text{(A6)}$$

We extract D_e by fitting the τ^{-1}_{ee} from Eq. (A5), then by adding $(D_e/\hbar)(\pi k_B)^2(T_e^2 - T_0^2)$ to the room temperature results. See Ref. [16] for more details.

2. Transport properties

Ab initio calculations of resistivity were performed using a linearized Boltzmann equation with a full-band relaxation-time approximation (RTA), where the conductivity tensor is given by

$$\sigma = \rho^{-1} = \int_{\text{BZ}} \frac{e^2 d\mathbf{k}}{(2\pi)^3} \sum_n \frac{\partial f_{\mathbf{k}n}}{\varepsilon_{\mathbf{k}n}} (v_{\mathbf{k}n} \otimes v_{\mathbf{k}n}) \left(\tau^{\text{MR}}_{\text{e-ph}}\right)_{\mathbf{k}n}. \quad \text{(A7)}$$

We then evaluate mobility using $\mu = \sigma/(ne)$, where n is the carrier density.

3. Phonon-mediated electron-electron scattering

Electron-electron scattering rate of electron in state $\mathbf{k}a$ as mediated by a virtual phonon is given by Fermi's golden rule,

$$\left(\tau^{\text{ph}}_{\text{ee}}\right)^{-1}_{\mathbf{k}a} = \frac{2\pi}{\hbar} \sum_{bcd} \int \frac{\Omega d\mathbf{q}}{(2\pi)^3} \int \frac{g_s \Omega d\mathbf{k}'}{(2\pi)^3} \left|M^{\mathbf{qkk}'}_{abcd}\right|^2 \times [f_{\mathbf{k}c} f_{(\mathbf{k}+\mathbf{q})b} + f_{(\mathbf{k}'+\mathbf{q})d}(1 - f_{\mathbf{k}'c} - f_{(\mathbf{k}+\mathbf{q})b})] \times \delta(\varepsilon_{\mathbf{k}a} + \varepsilon_{(\mathbf{k}'+\mathbf{q})d} - \varepsilon_{\mathbf{k}'c} - \varepsilon_{(\mathbf{k}+\mathbf{q})b}), \quad \text{(A8)}$$

with a second-order matrix element,

$$M^{\mathbf{qkk'}}_{abcd} \equiv \sum_a \frac{g^{\mathbf{q}\alpha *}_{\mathbf{k}a,(\mathbf{k}+\mathbf{q})b} g^{\mathbf{q}\alpha}_{\mathbf{k}'c,(\mathbf{k}'+\mathbf{q})d}}{\hbar\omega_{\mathbf{q}\alpha} + \varepsilon_{\mathbf{k}a} - \varepsilon_{(\mathbf{k}+\mathbf{q})b} + i\eta}. \quad \text{(A9)}$$

For transport properties, we only require $\mathbf{k}a$ near the Fermi level, typically weighted by $(-f'(\varepsilon_{\mathbf{k}a}))$ in Boltzmann RTA. We therefore define a Fermi-surface averaged phonon-mediated e-e scattering rate:

$$\begin{aligned}\left(\tau^{\mathrm{ph}}_{\mathrm{ee}}\right)^{-1} = {} & \frac{2\pi}{\hbar g(\varepsilon_F)} \sum_{abcd} \int \frac{\Omega d\mathbf{q}}{(2\pi)^3} \int \frac{g_s \Omega d\mathbf{k}'}{(2\pi)^3} \left|M^{\mathbf{qkk'}}_{abcd}\right|^2 \\ & \times (-f'(\varepsilon_{\mathbf{k}a}))[f_{\mathbf{k}c} f_{(\mathbf{k}+\mathbf{q})b} \\ & + f_{(\mathbf{k}'+\mathbf{q})d}(1 - f_{\mathbf{k}'c} - f_{(\mathbf{k}+\mathbf{q})b})] \\ & \times \delta(\varepsilon_{\mathbf{k}a} + \varepsilon_{(\mathbf{k}'+\mathbf{q})d} - \varepsilon_{\mathbf{k}'c} - \varepsilon_{(\mathbf{k}+\mathbf{q})b}). \quad \text{(A10)}\end{aligned}$$

Substituting the matrix element, dropping off-diagonal terms in the expansion of the square (phonon RPA), and introducing an auxiliary frequency integral to split the energy-conserving δ function into a, b and c, d parts, we can factorize and simplify the above to

$$\begin{aligned}\left(\tau^{\mathrm{ph}}_{\mathrm{ee}}\right)^{-1} = {} & \frac{2\pi\beta^{-1}}{g(\varepsilon_F)} \int \frac{d\omega}{\mathrm{sinch}^2\left(\frac{\beta\hbar\omega}{2}\right)} \\ & \times \sum_a \int \frac{\Omega d\mathbf{q}}{(2\pi)^3} \frac{G^2_{\mathbf{q}\alpha}}{|\hbar(\omega_{\mathbf{q}\alpha} - \omega) + i\eta|^2}, \quad \text{(A11)}\end{aligned}$$

where $\beta = (k_B T)^{-1}$ and $\mathrm{sinch}(x) \equiv \sinh(x)/x$. Above,

$$\begin{aligned}G_{q\alpha} \equiv {} & \sum_{ab} \int \frac{g_s \Omega d\mathbf{k}}{(2\pi)^3} \left|g^{\mathbf{q}\alpha}_{\mathbf{k}a,(\mathbf{k}+\mathbf{q})b}\right|^2 \\ & \times \delta(\varepsilon_{\mathbf{k}a} - \varepsilon_F)\delta(\varepsilon_{(\mathbf{k}+\mathbf{q})b} - \varepsilon_F) \quad \text{(A12)}\end{aligned}$$

is the (dimensionless) Fermi-surface integrated electron-phonon coupling for each phonon mode, which is essentially the weight of each phonon mode in the Eliashberg spectral function,

$$\alpha^2 F(\omega) = \frac{1}{g(\varepsilon_F)} \sum_\alpha \int \frac{\Omega d\mathbf{q}}{(2\pi)^3} \delta(\omega - \omega_{\mathbf{q}\alpha}) G_{\mathbf{q}\alpha}. \quad \text{(A13)}$$

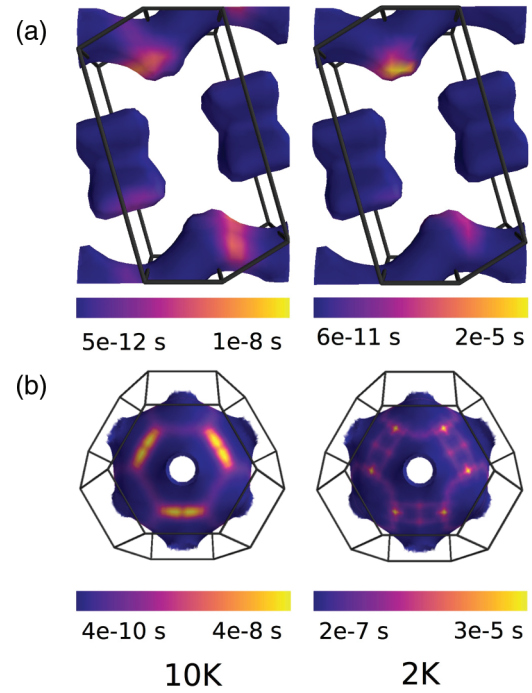

FIG. 5. Electron-phonon lifetimes projected onto the Fermi surfaces of (a) WP_2 and (b) copper at 10 and 2 K are shown to highlight the contrast in lifetime distribution order of magnitude between WP_2 and Cu.

In this form, we can use the standard Wannier e-ph approach to collect $G_{\mathbf{q}\alpha}$ for each phonon mode, analogous to the calculations of electron-phonon rates above. Using the collected $G_{\mathbf{q}\alpha}$ values, we can then evaluate the phonon-mediated electron-electron scattering rate using (A11), also using the phonon linewidth $\eta = \mathrm{Im}\bar{\omega}_{\mathbf{q}\alpha} = \pi\omega_{\mathbf{q}\alpha} G_{\mathbf{q}\alpha}$.

4. Comparison of Fermi surfaces

In addition to the averaged lifetime calculations in the main text, we consider the lifetime projected Fermi surfaces for copper corresponding to those reported in the manuscript for WP_2. In Fig. 5, we see that copper does feature high lifetime spots similar to those seen in WP_2 but distributed more evenly across the surface. We note that the particular difference in these surfaces is that the highest lifetime spots on the copper surface are 2 orders of magnitude longer, while those in WP_2 are a much more drastic 6 orders longer.

[1] A. Lucas and K. C. Fong, J. Phys.: Condens. Matter **30**, 053001 (2018).
[2] L. Levitov and G. Falkovich, Nat. Phys. **12**, 672 (2016).
[3] R. K. Kumar, D. A. Bandurin, F. M. D. Pellegrino, Y. Cao, A. Principi, H. Guo, G. H. Auton, M. B. Shalom, L. A. Ponomarenko, G. Falkovich, K. Watanabe, T. Taniguchi, I. V. Grigorieva, L. S. Levitov, M. Polini, and A. K. Geim, Nat. Phys. **13**, 1182 (2017).
[4] D. Bandurin, I. Torre, R. K. Kumar, M. B. Shalom, A. Tomadin, A. Principi, G. Auton, E. Khestanova, K. Novoselov, I. Grigorieva *et al.*, Science **351**, 1055 (2016).
[5] A. Junck, G. Refael, and F. von Oppen, Phys. Rev. B **90**, 245110 (2014).
[6] M. Mendoza, H. J. Herrmann, and S. Succi, Phys. Rev. Lett. **106**, 156601 (2011).
[7] P. J. W. Moll, P. Kushwaha, N. Nandi, B. Schmidt, and A. P. Mackenzie, Science **351**, 1061 (2016).

[8] C. Fu, T. Scaffidi, J. Waissman, Y. Sun, R. Saha, S. J. Watzman, A. K. Srivastava, G. Li, W. Schnelle, P. Werner, M. E. Kamminga, S. Sachdev, S. S. P. Parkin, S. A. Hartnoll, C. Felser, and J. Gooth, arXiv:1802.09468.

[9] J. Gooth, F. Menges, C. Shekhar, V. Süß, N. Kumar, Y. Sun, U. Drechsler, R. Zierold, C. Felser, and B. Gotsmann, arXiv:1706.05925.

[10] R. Mahajan, M. Barkeshli, and S. A. Hartnoll, Phys. Rev. B **88**, 125107 (2013).

[11] G. Autès, D. Gresch, M. Troyer, A. A. Soluyanov, and O. V. Yazyev, Phys. Rev. Lett. **117**, 066402 (2016).

[12] E. Razzoli, B. Zwartsenberg, M. Michiardi, F. Boschini, R. P. Day, I. S. Elfimov, J. D. Denlinger, V. Süß, C. Felser, and A. Damascelli, Phys. Rev. B **97**, 201103 (2018).

[13] R. Sundararaman, K. Letchworth-Weaver, K. Schwarz, D. Gunceler, Y. Ozhabes, and T. A. Arias, SoftwareX **6**, 278 (2017).

[14] R. Sundararaman, P. Narang, A. S. Jermyn, W. A. Goddard III, and H. A. Atwater, Nat. Commun. **5**, 12 (2014).

[15] A. Brown, R. Sundararaman, P. Narang, W. A. Goddard III, and H. A. Atwater, ACS Nano **10**, 957 (2016).

[16] A. M. Brown, R. Sundararaman, P. Narang, W. A. Goddard III, and H. A. Atwater, Phys. Rev. B **94**, 075120 (2016).

[17] A. M. Brown, R. Sundararaman, P. Narang, A. M. Schwartzberg, W. A. Goddard III, and H. A. Atwater, Phys. Rev. Lett. **118**, 087401 (2017).

[18] A. Jaoui, B. Fauqué, C. W. Rischau, A. Subedi, C. Fu, J. Gooth, N. Kumar, V. Süß, D. L. Maslov, C. Felser *et al.*, arXiv:1806.04094.

[19] R. Schönemann, N. Aryal, Q. Zhou, Y.-C. Chiu, K.-W. Chen, T. J. Martin, G. T. McCandless, J. Y. Chan, E. Manousakis, and L. Balicas, Phys. Rev. B **96**, 121108 (2017).

[20] N. Kumar, Y. Sun, N. Xu, K. Manna, M. Yao, V. Süss, I. Leermakers, O. Young, T. Förster, M. Schmidt, H. Borrmann, B. Yan, U. Zeitler, M. Shi, C. Felser, and C. Shekhar, Nat. Commun. **8**, 1642 (2017).

[21] A. Dal Corso, Comput. Mater. Sci. **95**, 337 (2014).

[22] A. M. Rappe, K. M. Rabe, E. Kaxiras, and J. D. Joannopoulos, Phys. Rev. B **41**, 1227 (1990).

[23] J. P. Perdew, A. Ruzsinszky, G. I. Csonka, O. A. Vydrov, G. E. Scuseria, L. A. Constantin, X. Zhou, and K. Burke, Phys. Rev. Lett. **100**, 136406 (2008).